J. Fluid Mech. (2020), *vol.* 891, A8. © The Author(s), 2020.
Published by Cambridge University Press
doi:10.1017/jfm.2020.114

Surface waves along liquid cylinders. Part 1. Stabilising effect of gravity on the Plateau–Rayleigh instability

Chi-Tuong Pham[1,†], **Stéphane Perrard**[2] **and Gabriel Le Doudic**[3]

[1]Université Paris-Saclay, CNRS, LIMSI, rue John von Neumann, 91400 Orsay, France

[2]Laboratoire de Physique de l'École normale supérieure, ENS, Université PSL, CNRS, Sorbonne Université, Université de Paris, 24 rue Lhomond, 75005 Paris, France

[3]Matière et Systèmes Complexes, Université de Paris, CNRS, 10 rue Alice Domon et Léonie Duquet, 75013 Paris, France

(Received 26 August 2019; revised 13 December 2019; accepted 3 February 2020)

We study the shape and the geometrical properties of sessile drops with translational invariance (namely 'liquid cylinders') deposited upon a flat superhydrophobic substrate. We account for the flattening effects of gravity on the shape of the drop using a pendulum rotation motion analogy. In the framework of the inviscid Saint-Venant equations, we show that liquid cylinders are always unstable because of the Plateau–Rayleigh instability. However, a cylindrical drop deposited upon a superhydrophobic non-flat channel (here, wedge-shaped channels) is stabilised beyond a critical cross-sectional area. The critical threshold of the Plateau–Rayleigh instability is analytically computed for various profiles of the channel. The stability analysis is performed in terms of an effective propagation speed of varicose waves. Experiments are performed in order to test these analytical results. We measure the critical drop size at which breakup occurs, together with the decreasing effective propagation speed of varicose waves as the threshold is approached. Our theoretical predictions are in excellent agreement with the experimental measurements.

Key words: breakup/coalescence, capillary flows, surface gravity waves

1. Introduction

Liquid cylinders, namely volumes of liquid of a given cross-section with translational invariance along its normal direction, have long been a matter of study, more specifically their stability, when surface tension is at play. Historically, in this context, the first reported experimental study of the destabilisation of a liquid column was due to Savart while studying the decay of liquid jets (Savart 1833). However, Savart did not mention surface tension as the driving phenomenon and Plateau was the first to interpret the destabilisation of a static circular column of liquid in terms of surface minimisation of the liquid interface (Plateau 1849, 1873). Lord Rayleigh then

† Email address for correspondence: pham@limsi.fr

performed a linear analysis of stability, computing the fastest axisymmetric growing mode of sinusoidal perturbations along its axis of a free infinite circular cylinder of inviscid liquid, confirming the values obtained by Plateau from the aforementioned experiments by Savart (Rayleigh 1878). In this framework, Lord Rayleigh stressed the fact that this now so-called Plateau–Rayleigh instability is independent of the general translatory motion of the jet. This first theoretical study was immediately followed by azimuthal perturbations of a circular cross-section (Rayleigh 1879). Later, the viscous properties of the liquid column were accounted for by Rayleigh (1892*a*,*b*), then followed by Tomotika who took the surrounding fluid into account (Tomotika 1935).

Ever since these seminal works on circular liquid cylinders, many studies regarding the problem of free liquid jets have been devoted to the instability of jets of various cross-section geometries (Gutmark & Grinstein 1999), including elliptical cross-section (Morris 1988; Amini & Dolatabadi 2011; Amini *et al.* 2014), rectangular cross-section (Tam & Thies 1992) or even star-shaped jets (Quinn 1992). However, these studies mostly concern high Reynolds number flows at which other physical phenomena such as vortex shedding or vorticity–surface interaction play a key role in the instability mechanism. At low Reynolds number, the pinch-off of a viscous elongated drop has been studied for various initial shapes by Stone & Leal (1989*a*,*b*).

In a different context, the Plateau–Rayleigh instability can also be encountered in the case of a free surface liquid cylinder constrained by the presence of a solid substrate along its longitudinal direction. For instance, the annular coating of a liquid on a wire or on the inside of a tube was first studied by Goren (1962). He related the fastest growing perturbation wavelength to the ratio of the two radii of the annulus and the Ohnesorge number.

Deposited upon a solid surface, a liquid cylinder is called a rivulet and it can undergo different instabilities such as capillary breakup (Schmuki & Laso 1990) or meandering for different wetting conditions: either hydrophobic conditions (Nakagawa & Scott 1984; Nakagawa 1992; Couvreur 2013), partial wetting (Birnir *et al.* 2008) or total wetting (Daerr *et al.* 2011); braiding (Mertens, Putkaradze & Vorobieff 2005); or splitting (Myers, Liang & Wetton 2004).

In the absence of longitudinal flow, liquid cylinders were called static rivulets, and the first theoretical study of their stability was due to Davis (1980). Using balance of kinetic energy arguments, he gave sufficient conditions for circular sessile cylinders to be stable, and he studied their stability for different contact angle conditions at a planar substrate (pinned contact line, constant contact angle, smooth contact angle variations with contact line speed).

Using a geometrical variational formulation, Sekimoto, Oguma & Kawasaki (1987) studied the shape and the instability of steady liquid ridges on a horizontal planar substrate, under partial wetting conditions, in a small slope approximation, and taking gravity into account. Speth & Lauga (2009) gave explicit calculations of unstable long-wave modes of a cylindrical ridge for pinned contact lines in the inviscid case. Within lubrication approximation, taking the gravity effects into account, together with the wetting conditions using a disjoining pressure model, Diez, González & Kondic (2009) analysed the stability of a rivulet on a horizontal plane. They evidenced the respective dependence of the instability on these effects and the nano- or macroscopic size of the rivulet. Recently, Bostwick & Steen (2018) performed, through a Rayleigh–Ritz method, a thorough study of the stability of inviscid sinuous and varicose modes, for pinned contact lines or free contact lines with constant contact angle. More specifically, they identified the dominant modes for various contact line configurations.

The case of non-planar substrates, in the context of a wedge-shaped groove, was first treated by Langbein (1990). Based on energy arguments, he showed that, depending on the contact angle and the opening angle of the wedge, static cylinders on a wedge-shaped groove could be stable or unstable. These results were extended by Roy & Schwartz (1999), considering various geometries of substrate and different wetting conditions. Using hydrodynamic considerations, the stability of a rivulet on a wedge was studied by Yang & Homsy (2007) in the flowing case (using lubrication approximation together with a model of dynamic contact line) and by Speth & Lauga (2009) in the static case (inviscid fluid, with pinned contact line wetting conditions). In the context of a circular constraint applied to one side of a cylindrical drop, Bostwick & Steen (2010) showed that this constraint slowed the growth rate of the unstable modes. In all aforementioned cases, gravity effects were not taken into account and circular cylindrical base states were considered.

As a summary, we can state that the Plateau–Rayleigh instability in liquid cylinders depends on the shape of the cross-section of the cylinder and on the wetting conditions when placed upon a substrate, either flat, wedge-shaped or curved. Moreover, the scale of the cross-section can reduce the critical wavenumber of the perturbations, beyond which the cylinder becomes stable: gravity, known to flatten sessile drops, has a stabilising effect on the Plateau–Rayleigh instability (Diez *et al.* 2009).

Note that the Plateau–Rayleigh instability can be fully inhibited to a certain extent in coated tubes because of gravitational drainage (Duclaux, Clanet & Quéré 2006). The stability of a liquid cylinder has also been studied for other liquid systems: ferromagnetic liquid cylinder stabilised by an orthoradial magnetic field (Arkhipenko *et al.* 1980); and soft solids for which the Plateau-Rayleigh instability can be inhibited by elastic forces (Mora *et al.* 2010).

Other examples of non-breaking slender liquid drops, without contact with any solid wall, have been observed in the case of liquid cylinders levitating above hot curved rectilinear substrates owing to the Leidenfrost effect (Perrard *et al.* 2015). Large volumes of liquid can be deposited above such substrates. Their lengths are several times larger than the perimeter of their cross-section, which contradicts the historical stability criterion proposed by Plateau (1849), stating that a – circular – slender drop breaks up whenever its length is larger than the circumference of its cross-section. In the study by Perrard *et al.*, Leidenfrost drops are flattened by gravity, which may play a significant stabilising role. If such drops are left evaporating without being water-fed the volume decreases down to a critical volume, at which breakup eventually occurs.

The current article will be devoted to the full characterisation of the shape of these flattened drops together with the characterisation of linear waves that the authors observed along these levitating liquid cylinders (here, restricting ourselves to the non-dispersive regime). To that end, we will consider – instead of a levitating liquid – a simpler system that can be viewed as geometrically equivalent: we will consider an infinite sessile cylinder deposited upon a superhydrophobic substrate.

The exact shape of the cross-section of such a drop will be obtained using a mechanical analogy with the rotation motion of a pendulum. We will relate the breakup of these drops to the Plateau–Rayleigh instability by studying the stability of varicose modes along these drops, resorting to a mass conservation and a section-averaged momentum equation, a formalism best known as the Saint-Venant equations, in an inviscid framework. We will show that the Plateau–Rayleigh instability is suppressed whenever the substrate underneath the drop becomes non-flat

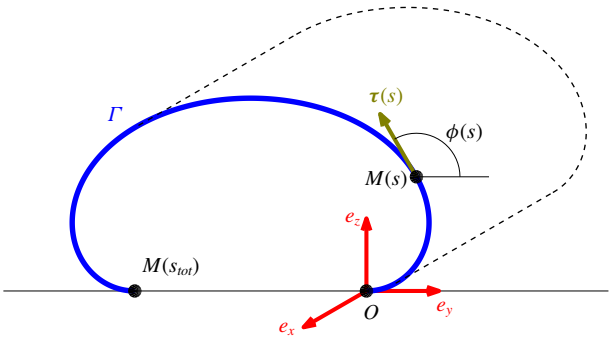

FIGURE 1. The shape of the free surface Γ of a cylindrical sessile drop placed upon a horizontal superhydrophobic substrate is computed. The drop profile is invariant along the x-direction. The border of the drop is parameterised by its arclength, s. The curve starts at the origin O (at which $s=0$) and ends at the point $M(s_{tot})$, with s_{tot} the total arclength. The tangent vector $\boldsymbol{\tau}$ at the point $M(s)$ forms an angle $\phi(s)$ with the horizontal.

and its cross-section is sufficiently large, which explains the observed stability of cylinders in Leidenfrost state (Perrard *et al.* 2015). In order to validate our predictions, experimental comparisons will be performed that show an excellent agreement, which confirms the validity of our approach in the non-dispersive limit.

In § 2, we present the computation of the exact shape of the cross-section of a sessile cylindrical drop, under superhydrophobic wetting conditions when placed upon a flat horizontal substrate. In § 3, we analyse the linear stability of such a drop using the Saint-Venant equations. We then present experimental comparisons with the theoretical results in § 4. Finally, in § 5, we close this paper with our conclusions and perspectives.

2. Shape of a cylindrical sessile drop

This section is devoted to the full characterisation of the shape of a sessile drop deposited upon a flat hydrophobic substrate, with translational invariance with respect to the x-direction, namely cylindrical sessile drops, taking gravity into account. To that end, we draw an analogy with the rotation motion of a pendulum and propose complete analytical expressions.

Let z denote the upward vertical direction and y the horizontal direction. The free interface will be denoted as Γ. It can be described as a curve in the (y, z)-plane (see figure 1). The latter will be parameterised by its arclength, s. The coordinates of a point $M(s)$ along the interface will be denoted as $(\eta(s), \zeta(s))$. At the point $M(s)$, the unit tangent vector $\boldsymbol{\tau}$ is given by $\boldsymbol{\tau} = \mathrm{d}M(s)/\mathrm{d}s$ and the transverse (that is the in-plane) curvature κ^t is given by $\mathrm{d}\boldsymbol{\tau}/\mathrm{d}s = \kappa^t \boldsymbol{n}$, where $\boldsymbol{n}$ is the unit normal vector. We set the angle $\phi(s)$ such that $\boldsymbol{\tau}(s) = \cos\phi(s)\boldsymbol{e}_y + \sin\phi(s)\boldsymbol{e}_z$, so that

$$\kappa^t = \frac{\mathrm{d}\phi}{\mathrm{d}s}, \quad \eta(s) = \eta_0 + \int_0^s \cos\phi(s)\,\mathrm{d}s, \quad \zeta(s) = \zeta_0 + \int_0^s \sin\phi(s)\,\mathrm{d}s. \qquad (2.1a\text{–}c)$$

In this section, by convention, the starting point of the curve $M(s=0) = (\eta_0, \zeta_0)$ will be located at the origin $O = (0, 0)$.

The equation satisfied by the vertical position ζ of the interface is obtained solving the hydrostatics equation, taking the Young–Laplace law into account. It reads (see,

for instance, Landau & Lifschitz (1987, § 61))

$$\rho g\zeta(s) + \sigma\kappa(s) = \mathcal{C}_0, \tag{2.2}$$

where σ denotes the surface tension and $\mathcal{C}_0$ is a constant independent of the x-coordinate.

We set the usual capillary length ℓ_c as $\ell_c^2 = \sigma/\rho g$. After differentiating (2.2) with respect to s, knowing that $\mathrm{d}\zeta/\mathrm{d}s = \sin\phi(s)$, we obtain

$$\frac{\mathrm{d}^2\phi}{\mathrm{d}s^2} + \frac{1}{\ell_c^2}\sin\phi(s) = 0, \tag{2.3}$$

which is equivalent to the classic equation of motion of a pendulum, where the time variable is now the arclength s. Equation (2.3) is equivalent to

$$\frac{1}{2}\left[\frac{\mathrm{d}\phi}{\mathrm{d}s}\right]^2 + \frac{1}{\ell_c^2}[1-\cos\phi(s)] = \text{const. } \mathcal{E} \quad \equiv \mathcal{H}(q,p), \tag{2.4}$$

with $\mathcal{H}$ the Hamiltonian of a pendulum of angular frequency $1/\ell_c$, for the time variable s and $(q,p) = (\phi, (\mathrm{d}\phi/\mathrm{d}s))$, the corresponding set of conjugate variables. As a conservative system, we have $\mathcal{H}(q(s),p(s)) = \mathcal{E}$, the conserved 'energy' along the time s, which only depends on the initial conditions $(\phi = \phi_i, (\mathrm{d}\phi/\mathrm{d}s) = \kappa_i^t)|_{s=s_i}$, at the given initial time s_i, so that

$$\mathcal{E} = \frac{1}{2}[\kappa_i^t]^2 + \frac{1}{\ell_c^2}[1-\cos\phi_i]. \tag{2.5}$$

The energy value $\mathcal{E}$ labels the different orbits of the autonomous dynamical system given by the corresponding Hamilton equations. The right-hand side part of the summation is bounded (corresponding to the ϕ-periodic potential energy of gravity), whereas the left-hand side part (corresponding to the kinetic energy, i.e. the curvature contribution) can assume arbitrary values.

Let us define $\mathcal{E}_c = 2/\ell_c^2$. The orbits corresponding to $\mathcal{E} = \mathcal{E}_c$ are the usual separatrices of the phase space, given by the equations

$$\kappa^t(\phi) = \frac{\mathrm{d}\phi}{\mathrm{d}s} = \pm\frac{2}{\ell_c}\cos\frac{\phi}{2}. \tag{2.6}$$

In terms of arclength s, ranging from $-\infty$ to $+\infty$, they read

$$\phi(s) = \mp\pi \pm 4\arctan\exp\left[\pm\frac{s}{\ell_c}\right] + 2k\pi \quad (k\in\mathbb{Z}). \tag{2.7}$$

The corresponding curves are displayed in figure 2. They partition the phase space into bounded regions (related to libration pendulum motion) and unbounded regions (related to rotation pendulum motion). In the framework of pendulum motion, they correspond to heteroclinic orbits, connecting neighbouring unstable equilibrium positions $\phi_k = (2k+1)\pi$, $k\in\mathbb{Z}$. We will later see that these separatrices correspond to the limit case of a sessile drop of infinite horizontal extension.

The orbits inside the separatrices ($\mathcal{E} < \mathcal{E}_c$) are closed. They correspond to libration modes in terms of pendulum. They are related to the shape of the cross-section of a

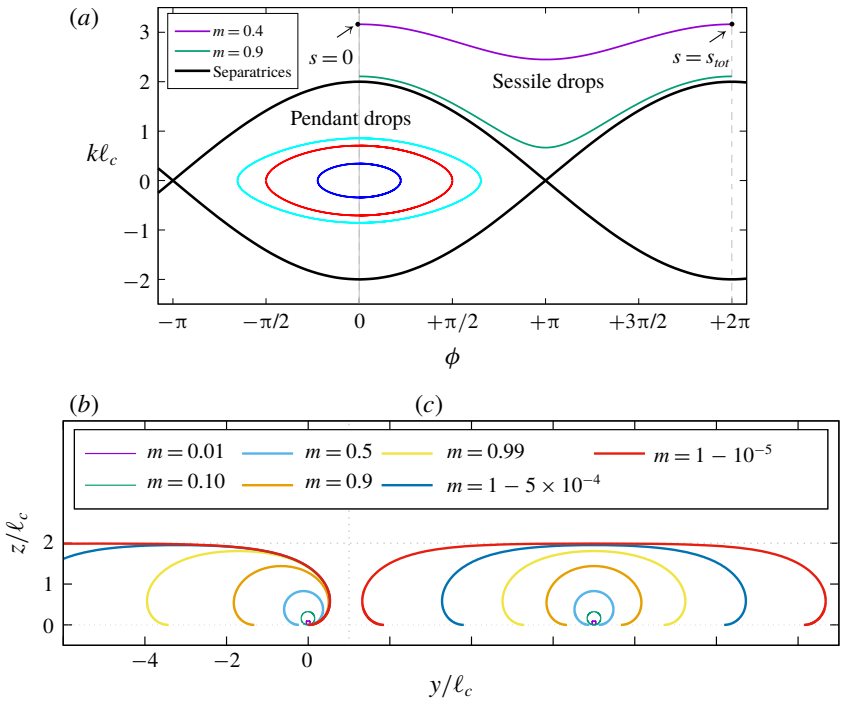

FIGURE 2. Cylindrical drop shapes viewed as pendulum orbits. (*a*) Phase space and typical orbits. The separatrices ($\mathcal{E} = \mathcal{E}_c$, see text for definition) partition the phase space into two types of regions. The bounded regions are those related to closed pendulum orbits (libration mode); they correspond to pendant drop profiles. Outside the separatrices, the orbits are those of pendulum rotation mode; they correspond to sessile drop profiles. In the case of superhydrophobic wetting conditions, the orbits start at $\phi = 0$ at arclength $s = 0$ and end at $\phi = 2\pi$ at arclength s_{tot} (see (2.13)). Two orbits are displayed, corresponding to parameters $m = 0.4$ and $m = 0.9$. (*b*) Drop shapes for different values of m, calculated starting at the origin O. The closer m is to the value 1, the larger the drop. In this limit, its height approaches $2\ell_c$. In contrast, the drops are nearly circles when m approaches zero. (*c*) Same drops, but centred with respect to their vertical symmetry axis.

pendant drop (with translational invariance along the x-direction). One can refer to the comprehensive review of McCuan (2017) for the properties and the explicit analytical expressions of the solutions. Note that the pendulum analogy was previously made by Roman, Gay & Clanet (2003) as well. Nevertheless, only numerical solutions were proposed by the authors.

In the following, we will resort to the usual partial and complete elliptic integrals (for any parameter $m < 1$) defined as

$$E(\phi|m) = \int_0^\phi \sqrt{1 - m\sin^2 x}\,\mathrm{d}x, \quad E(m) = \int_0^{\pi/2} \sqrt{1 - m\sin^2 x}\,\mathrm{d}x, \tag{2.8a,b}$$

$$F(\phi|m) = \int_0^\phi \frac{\mathrm{d}x}{\sqrt{1 - m\sin^2 x}}, \quad K(m) = \int_0^{\pi/2} \frac{\mathrm{d}x}{\sqrt{1 - m\sin^2 x}}. \tag{2.9a,b}$$

The solutions to our system are those corresponding to $\mathcal{E} > \mathcal{E}_c$, namely orbits outside the separatrices. They are related to the rotating modes of a pendulum. If we set m,

the parameter such that

$$\frac{\mathcal{E}_c}{\mathcal{E}} \overset{\text{def}}{=} m < 1, \tag{2.10}$$

we have κ^t, the transverse curvature, given by the equation

$$\kappa^t(\phi) = \frac{\mathrm{d}\phi}{\mathrm{d}s} = \pm \frac{2}{\ell_c \sqrt{m}} \sqrt{1 - m \sin^2 \frac{\phi}{2}} \tag{2.11}$$

that yields the solution

$$\phi(s) = 2 \arcsin \left[\mathrm{sn} \left(\frac{s}{\ell_c \sqrt{m}}; m \right) \right], \tag{2.12}$$

with the proper determination of arcsin function and sn, the Jacobi elliptic function of parameter m ($\phi(s)$ can be expressed in terms of am amplitude function as well). For a given m, the total arclength s_{tot} is given by

$$s_{tot}(m) = \frac{\ell_c \sqrt{m}}{2} \int_0^{2\pi} \frac{\mathrm{d}\phi}{\sqrt{1 - m \sin^2 \frac{\phi}{2}}} = 2 \ell_c \sqrt{m}\, K(m) \tag{2.13}$$

and the orbits in the phase space are given by the following parameterisation with angle ϕ:

$$\eta(\phi) = \frac{\ell_c}{2} \sqrt{m} \int_0^{\phi} \mathrm{d}\varphi \, \frac{\cos \varphi}{\sqrt{1 - m \sin^2 \frac{\varphi}{2}}}, \quad \zeta(\phi) = \frac{\ell_c}{2} \sqrt{m} \int_0^{\phi} \mathrm{d}\varphi \, \frac{\sin \varphi}{\sqrt{1 - m \sin^2 \frac{\varphi}{2}}}. \tag{2.14a,b}$$

The explicit expressions of $\eta(\phi)$ and $\zeta(\phi)$ then read

$$\eta(\phi) = \frac{2\ell_c}{\sqrt{m}} \left[E\left(\frac{\phi}{2} \middle| m \right) - \left(1 - \frac{m}{2} \right) F\left(\frac{\phi}{2} \middle| m \right) \right], \quad \zeta(\phi) = \frac{2\ell_c}{\sqrt{m}} \left[1 - \sqrt{1 - m \sin^2 \frac{\phi}{2}} \right]. \tag{2.15a,b}$$

Note that Lamb (1928, § 127) and Ku, Ramsey & Clinton (1968) previously gave the same expressions, using different parameterisations, but without resorting explicitly to a pendulum analogy, whereas Michael & Williams (1977) solved the same problem using numerical calculations.

In figure 2, we show various shapes of drops for different values of m (and the drop pictured in figure 1 corresponds to $m = 0.95$). One must keep in mind that the $m \to 0^+$-limit corresponds to vanishingly small droplets (i.e. high energy $\mathcal{E}$) whereas the limit case $m \to 1^-$ corresponds to large flattened drops (i.e. energy $\mathcal{E}$ close to $\mathcal{E}_c$, namely orbits close to the separatrices).

From (2.15), we can compute the following typical quantities.

(i) The vertical thickness of the drop, denoted as $\Delta Z_{max}(m)$, is given by

$$\Delta Z_{max}(m) = \zeta(\pi) - \zeta(0) = 2\ell_c \frac{1 - \sqrt{1 - m}}{\sqrt{m}} \tag{2.16}$$

and is upper-bounded by $2\ell_c$, which corresponds to the usual result that the maximum height of a liquid puddle is $2\ell_c$.

(ii) The transverse curvature at the top of the drop is given by

$$\kappa_{top}(m) = \frac{2}{\ell_c}\sqrt{\frac{1-m}{m}}. \tag{2.17}$$

Note that we have the following relationship, as a consequence of (2.2):

$$\frac{\mathcal{C}_0(m)}{\rho g \ell_c} = \frac{\Delta Z_{max}(m)}{\ell_c} + \ell_c \kappa_{top}(m) = \frac{2}{\sqrt{m}}. \tag{2.18}$$

(iii) The horizontal extension of the drop is given by

$$\Delta Y_{max} = \left[\eta\left(\frac{3\pi}{2}\right) - \eta\left(\frac{\pi}{2}\right)\right] \tag{2.19}$$

$$= \frac{2\ell_c}{\sqrt{m}}\left\{\left(1-\frac{m}{2}\right)\left[F\left(\frac{\pi}{4}\middle|m\right) - F\left(\frac{3\pi}{4}\middle|m\right)\right] + \left[E\left(\frac{3\pi}{4}\middle|m\right) - E\left(\frac{\pi}{4}\middle|m\right)\right]\right\}. \tag{2.20}$$

(iv) The cross-sectional area of the drop is given by

$$\mathscr{A}(m) = -\int_\Gamma \zeta \,\mathrm{d}\eta = -\int_0^{2\pi} \zeta(\phi)\frac{\mathrm{d}\eta}{\mathrm{d}\phi}(\phi)\,\mathrm{d}\phi,$$

$$= \frac{8\ell_c^2}{m}\left[\left(1-\frac{m}{2}\right)K(m) - E(m)\right]. \tag{2.21}$$

(v) The contact extension at the substrate is given by

$$\Lambda_c(m) = [\eta(0) - \eta(2\pi)] = -\frac{\ell_c}{2}\sqrt{m}\int_0^{2\pi} \frac{\cos\varphi}{\sqrt{1 - m\sin^2\dfrac{\varphi}{2}}}\,\mathrm{d}\varphi \tag{2.22}$$

and we have the following relationship between $\Lambda_c(m)$ and $\mathscr{A}(m)$:

$$\mathscr{A}(m) = \frac{2}{\sqrt{m}}\ell_c \Lambda_c(m), \tag{2.23}$$

which yields

$$\Lambda_c(m) = \frac{4\ell_c}{\sqrt{m}}\left[\left(1-\frac{m}{2}\right)K(m) - E(m)\right]. \tag{2.24}$$

Note that we have exhibited the shape of a cylindrical drop deposited upon a superhydrophobic flat substrate (i.e. imposing a contact angle $\theta_c = \pi$) that corresponds to an orbit starting from angle $\phi = 0$ and ending at angle $\phi = 2\pi$. In a more general case, if the drop is deposited upon a horizontal substrate at which the corresponding contact angle is θ_c, the shape of the interface then corresponds to a symmetric portion of the same kind of orbit, with an angle ϕ ranging from $\pi - \theta_c$ to $\pi + \theta_c$, allowing us to recover analytically the shape of a static rivulet previously numerically computed by Myers *et al.* (2004). We will resort to an analogous statement in § 3.5, where a wedge-shaped substrate will be considered. We now turn to a couple of asymptotic cases, for which the expressions can be greatly simplified and will be of use thereafter.

2.1. *Small values of m regime (nearly circular drop)*

For small values of positive parameter m, we have the following expansions:

$$\Delta Z_{max}(m) \underset{m\to 0^+}{=} \ell_c\sqrt{m}\left[1+\tfrac{1}{4}m+O(m^2)\right], \tag{2.25}$$

$$\Delta Y_{max}(m) \underset{m\to 0^+}{=} \ell_c\sqrt{m}\left[1+\frac{1}{4}\left(1+\frac{\pi}{4}\right)m+O(m^2)\right], \tag{2.26}$$

$$\mathscr{A}(m) \underset{m\to 0^+}{=} \frac{\pi}{4}m\ell_c^2+O(m^2). \tag{2.27}$$

Therefore, the cross-section of the drop is nearly that of a circle of radius R_0 that reads at leading order

$$R_0(m)=\tfrac{1}{2}\sqrt{m}\ell_c \underset{m\to 0^+}{=} \tfrac{1}{2}\Delta Z_{max} \underset{m\to 0^+}{=} \tfrac{1}{2}\Delta Y_{max} \tag{2.28}$$

and a contact length to the substrate $\Lambda_c(m)$ that satisfies

$$\Lambda_c \underset{m\to 0^+}{=} \frac{\pi}{8}m^{3/2}\ell_c \tag{2.29}$$

which is then negligible compared to the radius $R_0(m)$. As the volume per unit length (in the x-direction) increases, we depart from the circular shape because of gravity that flattens the drop.

2.2. *Parameter m close to* 1^- *(flattened drop)*

Let the parameter μ be such that $m=1-\mu$. We can compute the following asymptotic expressions for $\mu\to 0^+$ that read:

$$\Delta Z_{max}(m) \underset{\mu\to 0^+}{=} 2\ell_c\left[1-\sqrt{\mu}+o(\sqrt{\mu})\right], \tag{2.30}$$

$$\Delta Y_{max}(m) \underset{\mu\to 0^+}{=} \ell_c\left[-\log\mu+\left(-4+2\sqrt{2}+2\log\tan\frac{\pi}{8}+4\log 2\right)\right]+O(\mu\log\mu), \tag{2.31}$$

$$\mathscr{A}(m) \underset{\mu\to 0^+}{=} 2\ell_c^2[-\log\mu+4(\log 2-1)]+O(\mu\log\mu), \tag{2.32}$$

$$\Lambda_c(m)=\frac{\sqrt{m}}{2\ell_c}\mathscr{A}(m) \underset{\mu\to 0^+}{=} \ell_c[-\log\mu+4(\log 2-1)]+O(\mu\log\mu), \tag{2.33}$$

with the following approximate numerical values of the additive constants to the logarithmic expressions, found in (2.31) and (2.33),

$$\mathscr{C}_1=-4+2\sqrt{2}+2\log\tan\frac{\pi}{8}+4\log 2\simeq -0.16173, \tag{2.34}$$

$$\mathscr{C}_2=4(\log 2-1)\simeq -1.2274. \tag{2.35}$$

Last, note that we have the following relationship between the value of the cross-sectional area and those of the vertical thickness and the contact extension

$$\mathscr{A}(m) \underset{\mu\to 0^+}{=} \Lambda_c(m)\times\Delta Z_{max}(m)\left[1-\sqrt{\mu}+O(\mu)\right], \tag{2.36}$$

and we have $\ell_c/2(\mathscr{C}_1-\mathscr{C}_2)$, corresponding roughly to half the capillary length, which is the length of the tip of the drop protruding above the wetted area.

In figure 3, we plot ΔZ_{max}, ΔY_{max} together with the aspect ratio $\varrho_A=\Delta Y_{max}/\Delta Z_{max}$. The latter is always larger than 1 and diverges in the limit $m\to 1^-$ as ΔY_{max} does. The plots are given with respect to the coordinate m or $\mu=1-m$, in lin–lin or log–lin scales.

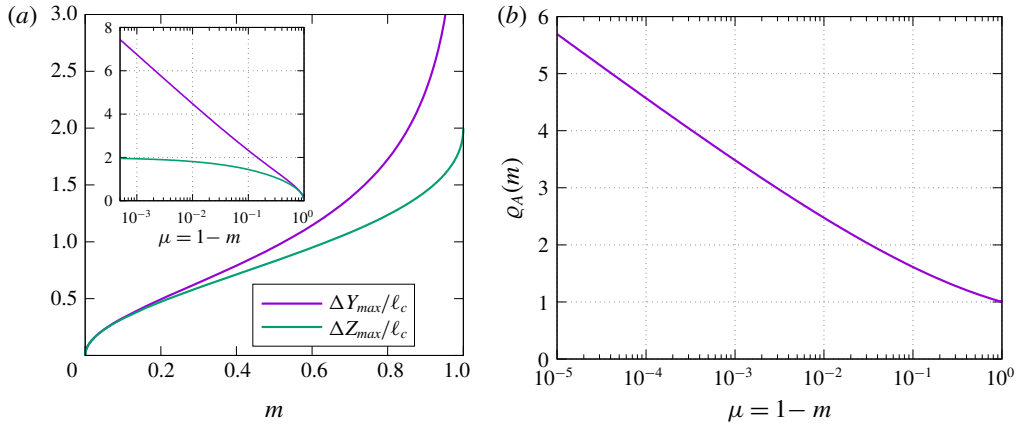

FIGURE 3. (*a*) Plot of the horizontal extension ΔY_{max} and the thickness ΔZ_{max} with respect to the variables m and $\mu = 1 - m$ (inset); the y-coordinates are expressed in ℓ_c-units. (*b*) Plot of the aspect ratio $\varrho_A(m) = \Delta Y_{max}/\Delta Z_{max}$ with respect to $\mu = 1 - m$. For $m \to 0$ (or $\mu \to 1$), the cross-section of the cylinder is nearly a circle, whereas for $m \to 1$ (or $\mu \to 0$), the horizontal extension diverges and the thickness tends to $2\ell_c$.

3. Plateau–Rayleigh instability in the Saint-Venant equations framework

In the previous section, the shape of a sessile cylindrical drop was calculated when placed upon a horizontal planar substrate with non-wetting conditions; typical dimensions were also obtained. In this section, the question of their stability against varicose perturbation is dealt with. It is related to the classical Plateau–Rayleigh instability in the context of non-circular geometry. To that end, we will use the inviscid Saint-Venant equations and focus on the speed of propagation of varicose waves along our sessile cylinder placed upon a superhydrophobic substrate. We will show that such drops can become stable provided the substrate is non-flat and sufficiently large.

3.1. *Saint-Venant governing equations*

The Saint-Venant equations are a set of hyperbolic equations that were proposed by the eponymous Saint-Venant (1871) in order to study flows in open-channels along the x-direction. Their derivation is based on a long-wavelength (shallow water limit $k \to 0$) expansion and the basic hypotheses are the following: (i) the flow is considered quasi-parallel in the x-direction; and (ii) the pressure is hydrostatic. Under these hypotheses, if one sets the following quantities:

$$S(x, t), \quad \text{the transverse cross-sectional area of liquid,} \tag{3.1}$$

$$\bar{u}(x, t) = \frac{1}{S(x, t)} \int_{S(x,t)} u(x, y, z, t)\, \mathrm{d}y\, \mathrm{d}z, \quad \text{the section-averaged velocity,} \tag{3.2}$$

$$P(x, y, z, t), \quad \text{the hydrostatic three-dimensional pressure field,} \tag{3.3}$$

the inviscid Saint-Venant equations read

$$\partial_t S + \partial_x (S\bar{u}) = 0, \tag{3.4}$$

$$\partial_t \bar{u} + \bar{u}\partial_x \bar{u} + \frac{1}{S(x,t)} \int_{S(x,t)} \frac{1}{\rho} \frac{\partial}{\partial x}[P(x,y,z,t)]\,\mathrm{d}y\,\mathrm{d}z = 0. \tag{3.5}$$

This set of equations is expressed in terms of section-averaged pressure gradient in the x-coordinate and turns into one-dimensional equations in space. For a complete derivation of these equations (including viscous effects), one can read the article of Decoene *et al.* (2009). As we are interested in the linear stability of a sessile drop, we will study a linearised version of these equations.

3.2. *Special case of triangle-shaped cross-section*

As a first elementary result given by the Saint-Venant equations, let us neglect the surface tension effects and consider a triangular cross-section of liquid, with both sides Γ_α and Γ_β, respectively, making an angle α and β with the horizontal. As no capillary effects are considered, we consider a flat horizontal interface. Let $S(x,t)$ be the cross-sectional area at coordinate x. We have $S(x,t) = \frac{1}{2}\lambda H^2(x,t)$, with H, the liquid depth measured from the bottom of the substrate and $\lambda = \frac{1}{2}(\sin(\alpha+\beta)/\sin\alpha\sin\beta)$. We denote as S_0, the liquid cross-sectional area at rest and as H_0, its corresponding depth. The pressure field is hydrostatic, hence it is independent of the y-coordinate and reads

$$P(x,y,z,t) = \rho g[H(x,t) - z]. \tag{3.6}$$

The Saint-Venant equations (3.4) and (3.5) after linearisation then read

$$\partial_t S + \partial(S\bar{u}) = 2\lambda H_0 \partial_t H + S_0 \partial_x \bar{u} = 0, \tag{3.7}$$

$$\partial_t \bar{u} + \frac{1}{S}\int_S \frac{1}{\rho}(\partial_x P)\,\mathrm{d}y\,\mathrm{d}z = \partial_t \bar{u} + g\partial_x H = 0, \tag{3.8}$$

so that we obtain the following wave equation on H

$$\partial_{tt} H - \tfrac{1}{2} g H_0 \partial_{xx} H = 0, \tag{3.9}$$

hence the gravity wave speed

$$c_0 = \sqrt{\frac{gH_0}{2}}. \tag{3.10}$$

3.3. *Adiabatic perturbation hypothesis and discussion*

In this article, we will make the following strong hypothesis: at any coordinate x, at any time t, we will assume that the cross-section shape (of area value $S(x,t)$) is adiabatically given by the equilibrium static shape calculated in § 2, at that very value $S(x,t)$, corresponding to a geometrical parameter $m(x,t)$. This assumption implies that the contact line is free to move on the superhydrophobic substrate, with contact angle at the substrate kept constant at value π. Moreover, we assume that the pressure field remains hydrostatic, hence independent of the y-coordinate.

In the current situation, translational invariance in the x-direction does not hold any longer so that the constant $\mathcal{C}_0$ given by (2.2) must depend on the coordinate x and time t. In the framework of our assumption, the shape corresponds to that at equilibrium, provided it is given by some parameter $m(x,t)$ and we have

$$\mathcal{C}_0(x,t) = \rho g \zeta(x,s,t) + \sigma \kappa^t(x,s,t) \tag{3.11}$$

at given x and t, all along the interface, namely for all $s \in [0, s_{tot}(x, t)]$. It can be calculated anywhere along the interface. In the following, we will choose to calculate it at the top of the drop, i.e. at angle $\phi = \pi$, at which we have $\zeta(\pi) = \Delta Z_{max}(m(x, t))$ and $\kappa^t(x, s, t) = \kappa_{top}(m(x, t))$, respectively, given by (2.16) and (2.17).

Let us now focus on the hydrostatic pressure field. *A priori*, for a point of coordinates (x, y, z) inside the drop, its expression reads, because of the Young–Laplace law and (3.11)

$$P(x, y, z, t) = \rho g[\zeta(x, s, t) - z] + \sigma\kappa^t(x, s, t) + \sigma\kappa^l(x, s, t), \tag{3.12}$$

$$= \mathcal{C}_0(x, t) - \rho g z + \sigma\kappa^l(x, s, t), \tag{3.13}$$

with s being an arclength coordinate satisfying $\eta(s, t) = y$ and the curvature term being the sum of the transverse curvature $\kappa^t(x, s, t)$ (i.e. in the (y, z)-plane) and the longitudinal curvature $\kappa^l(x, s, t)$ (i.e. in the x-direction) at a given point of coordinates (x, s, t) located at the interface. At this stage, note that, because of the possible values of s, the pressure P can be bivalued.

The adiabatic hypothesis regarding the equilibrium shape is valid in the limit $\kappa^t \gg \kappa^l$, which corresponds to the long-wave limit. Without entering into further technical details, at linear approximation, the longitudinal curvature term $\kappa^l(x, s, t)$ will yield second-order contributions in x-derivatives of $S(x, t)$ in the expression of the pressure P, whereas $C_0(x, t)$ only involves zeroth-order contributions in x-derivatives of $S(x, t)$. Therefore, in the following, we will not account for the presence of κ^l and will then solely focus on the terms that will have non-dispersive contributions in the dispersion relation we are looking for. The section-averaged value of $\partial_x P$ used in the Saint-Venant equations then reads

$$\frac{1}{S(x, t)} \int_{S(x,t)} \{\partial_x P(x, y, z, t)\} \, \mathrm{d}y \, \mathrm{d}z = \frac{1}{S(x, t)} \int_{S(x,t)} \{\partial_x \mathcal{C}_0(x, t)\} \, \mathrm{d}y \, \mathrm{d}z = \partial_x \mathcal{C}_0(x, t). \tag{3.14}$$

3.4. *Plateau–Rayleigh instability in drops on flat hydrophobic substrate*

We now turn to the stability study of the static sessile drops considered in § 2. As mentioned in § 3.3, we consider one particular class of perturbation by making the following assumption: the cross-section shape – of transverse area value $S(x, t)$ – is adiabatically given by the equilibrium static shape calculated in § 2, at that very value $S(x, t)$, corresponding to a geometrical parameter $m(x, t)$, at any given space coordinate x and time t. The contact line is then free to move on the superhydrophobic substrate, keeping a constant contact angle equal to π. We focus on the varicose deformations; the liquid is supposed inviscid. Moreover, we choose the particular class of varicose perturbations with a symmetry about its (x, z)-mid-plane, as displayed in figure 2(*c*). The base state is supposed to correspond to the parameter m_0, with a cross-sectional area equal to $S_0 = S(m_0)$.

We set the perturbed cross-sectional area as being $S(x, t) = S_0 + \varsigma(x, t)$, with $\varsigma \ll S_0$ and set $\bar{u}$ as the section-averaged velocity. Because of (3.14), the section-averaged value of $\partial_x P$ can be expressed as

$$\partial_x \bar{p} = \rho g \partial_x[\Delta Z_{max}(x, t)] + \sigma \, \partial_x[\kappa_{top}(x, t)]. \tag{3.15}$$

The linearised Saint-Venant equations then read

$$\partial_t \varsigma + S_0 \, \partial_x \bar{u} = 0, \tag{3.16}$$

$$\partial_t \bar{u} + \frac{1}{\rho} \partial_x \bar{p} = 0, \tag{3.17}$$

that is,

$$\partial_{tt}\varsigma = \frac{S_0}{\rho}\partial_{xx}\bar{p}. \tag{3.18}$$

Knowing that

$$\partial_x[\Delta Z_{max}(x,t)] = \left[\frac{\partial[\Delta Z_{max}]}{\partial m}\right]\left[\frac{\partial S}{\partial m}\right]^{-1}\left[\frac{\partial S}{\partial x}\right], \tag{3.19}$$

$$\partial_x[\kappa_{top}(x,t)] = \left[\frac{\partial \kappa_{top}}{\partial m}\right]\left[\frac{\partial S}{\partial m}\right]^{-1}\left[\frac{\partial S}{\partial x}\right], \tag{3.20}$$

we obtain the following wave equation, after only retaining the linear contributions of ς:

$$\partial_{tt}\varsigma = g\left[\frac{S_0}{\dfrac{\partial S}{\partial m}(m_0)}\right]\left\{\left[\frac{\partial[\Delta Z_{max}]}{\partial m}(m_0)\right] + \frac{\sigma}{\rho g}\left[\frac{\partial \kappa_{top}}{\partial m}(m_0)\right]\right\}\partial_{xx}\varsigma. \tag{3.21}$$

Setting $\varsigma(x,t) = \varepsilon\exp[\mathrm{i}(\omega t - kx)]$ eventually yields the following dispersion relation:

$$\omega^2(k) = gk^2\left[\frac{S_0}{\dfrac{\partial S}{\partial m}(m_0)}\right]\left\{\left[\frac{\partial[\Delta Z_{max}]}{\partial m}(m_0)\right] + \ell_c^2\left[\frac{\partial \kappa_{top}}{\partial m}(m_0)\right]\right\}. \tag{3.22}$$

We have an instability whenever $\omega^2(k) < 0$; conversely, if $\omega^2(k) > 0$, the varicose mode is stable.

Let the following dimensionless quantities be

$$a(m_0) = \left[\frac{S_0}{\dfrac{\partial S}{\partial m}(m_0)}\right] = 2m_0(1-m_0)\frac{(m_0-2)K(m_0)+2E(m_0)}{(m_0-4)(m_0-1)K(m_0)+(3m_0-4)E(m_0)}, \tag{3.23}$$

$$b(m_0) = \frac{1}{\ell_c}\left[\frac{\partial[\Delta Z_{max}]}{\partial m}(m_0)\right] + \ell_c\left[\frac{\partial \kappa_{top}}{\partial m}(m_0)\right] = -{m_0}^{-3/2}, \tag{3.24}$$

we then obtain the dispersion relation, that reads

$$\omega^2(k) = g\ell_c k^2[a(m_0)]\,[b(m_0)], \tag{3.25}$$

which yields the expression of the wave speed

$$c_{eff}^2(m_0) = g\ell_c[a(m_0)]\,[b(m_0)]. \tag{3.26}$$

This quantity is always negative because of the factor $b(m_0)$ (see (3.24)), so that a cylindrical sessile drop on a flat superhydrophobic substrate is always unstable regardless of its size. As a visual illustration, in figure 4, we plot the quantities $a(m)$ and $c_{eff}^2/(g\ell_c) = a(m)\,b(m)$ as functions of the parameter m.

In the following, we will make more quantitative statements, by analysing these results in two distinct limits: small m regime, i.e. small cross-section cylinder and large m regime (m close to 1^-), i.e. large cross-section regime.

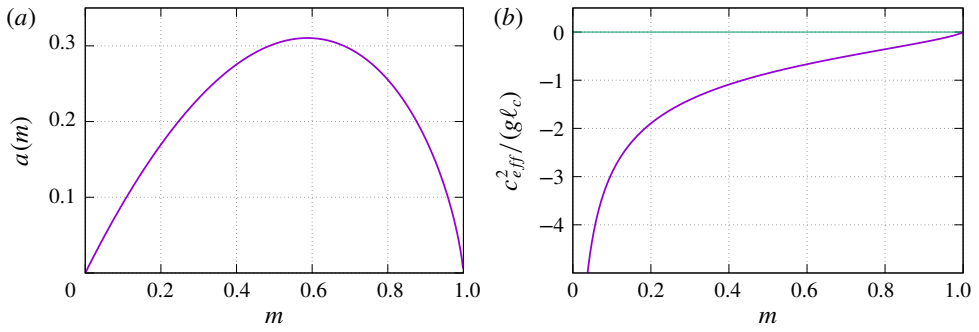

FIGURE 4. Plots of (*a*) the coefficients $a(m)$ together with (*b*) the renormalised $c^2_{eff}/(g\ell_c) = a(m)\,b(m)$ with respect to the parameter m. The values of c^2_{eff} are always negative, therefore, the drop is unstable. The larger m, the smaller the growth rate. In the limit $m \to 1^-$, we have $c^2_{eff} \to 0^-$; in this regime, the horizontal extension of the cylinder tends to infinity and the latter becomes marginally unstable.

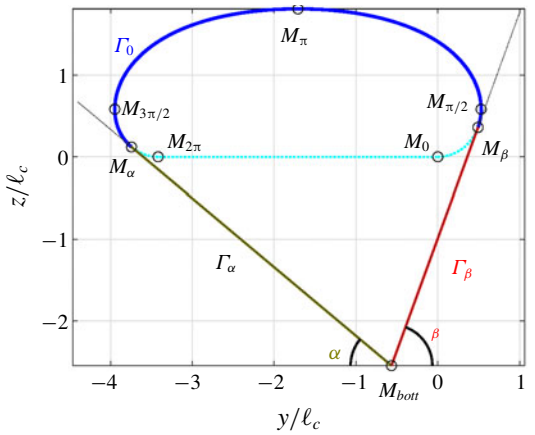

FIGURE 5. Geometry of a sessile cylindrical drop deposited upon a wedge-shaped substrate with angles to the horizontal equal to α and β. In dashed cyan is superimposed the shape of a drop of same horizontal extension ΔY_{max}, deposited upon a flat superhydrophobic substrate. Eight particular points are shown (see § 3.5 for their definition). Here, Γ_0 denotes the free surface, while Γ_α and Γ_β correspond to the parts of the wedge wetted by the drop. They connect M_α to M_{bott} and M_{bott} to M_β, respectively.

3.4.1. *Small m regime: nearly circle cross-section, Plateau–Rayleigh instability recovered*

Let us consider the asymptotic regime $m \to 0^+$. We have

$$a(m) \underset{m\to 0^+}{=} m - \tfrac{3}{4}m^2 + O(m^3), \tag{3.27}$$

$$b(m) = -m^{-3/2}, \tag{3.28}$$

and the dispersion relation then reads

$$\omega^2(k, m) \underset{m\to 0^+}{\simeq} g\ell_c k^2 \left[-\frac{1}{\sqrt{m}}\right]. \tag{3.29}$$

We see that for small values of m, we have an instability corresponding to the classic Plateau–Rayleigh instability: rewriting this expression in terms of radius of the drop $R_0 = \frac{1}{2}\ell_c\sqrt{m}$ (see (2.28)) indeed leads to

$$\omega^2(k, R_0) \underset{m\to 0^+}{\simeq} -\frac{\sigma}{2\rho R_0^3}(kR_0)^2. \tag{3.30}$$

As a reminder, we recall that the growth rate Σ of the classic Plateau–Rayleigh instability in the case of a free cylinder of radius R_0 reads

$$\Sigma^2(k, R_0) = \frac{\sigma}{\rho R_0^3}\frac{\mathrm{I}_1(kR_0)}{\mathrm{I}_0(kR_0)}[1 - (kR_0)^2]kR_0, \tag{3.31}$$

with I_0 and I_1 the zeroth and first modified Bessel functions of the first kind, which satisfy for small x, $\mathrm{I}_0(x) \underset{x\to 0}{\sim} 1$ and $\mathrm{I}_1(x) \underset{x\to 0}{\sim} x/2$. The angular frequency ω satisfies the exact same properties as the growth rate Σ at small k, at leading quadratic order.

3.4.2. *Large cross-section regime*

For large cross-section drops, the Plateau–Rayleigh instability still holds, for $b(m)$ is always negative, for any $m \in\ ]0, 1[$ (see (3.24)). Still, let us be more quantitative. For $m = 1 - \mu$ with $\mu \to 0^+$, we have

$$a(\mu) = -\mu[\log(\mu) + 4(1 - \log(2))] + O(\mu^2), \tag{3.32}$$

$$b(\mu) \underset{\mu\to 0^+}{=} -1 - \frac{3\mu}{2} - \frac{15\mu^2}{8} + O(\mu^3), \tag{3.33}$$

so that the wave celerity reads

$$c_{eff}^2 \underset{\mu\to 0^+}{\simeq} g\ell_c\mu[\log(\mu) + 4(1 - \log 2)] \underset{\mu\to 0^+}{\longrightarrow} 0^-. \tag{3.34}$$

In the limit of very large cross-sectional areas, the growth rate vanishes and wide drops become marginally unstable. This result is reminiscent of the result evidenced by Diez *et al.* (2009), in a different wetting situation (partial wetting), who stated that, because of gravity, a rivulet was unstable for a reduced interval of small wavenumbers.

As a general conclusion to this subsection, a sessile cylindrical drop placed upon a superhydrophobic flat substrate is always unstable whatever its volume by unit length may be.

3.5. *Stabilisation due to substrate shape*

In this section, we will study the stability of our previous sessile drop, this time deposited upon a non-flat superhydrophobic substrate, more specifically, a substrate that has a wedge-shaped geometry. We will start with the general case and then focus on two particular geometries used in our experimental set-ups, as a comparison with theoretical results. This study will greatly depart from the studies regarding wedge-shaped substrates that were cited in the introduction (Langbein 1990; Roy & Schwartz 1999; Yang & Homsy 2007; Speth & Lauga 2009) because we account for gravity effects that will play a crucial role on stabilising sessile drops, as we will see.

The substrate that we consider is a wedge with angles to the horizontal equal to α and β. Without any loss of generality, we will assume that $0 < \alpha \leqslant \beta < \pi/2$.

When $\alpha = \beta$, the substrate is symmetric. The shape of the liquid domain will consist in a sessile liquid cap (Γ_0 will denote its boundary) connected to tangent straight lines of angle α and β with the horizontal, i.e. that of a (partial) sessile cap placed upon a triangular liquid cylinder, as depicted in figure 5. The sessile cap profile Γ_0 corresponds to a partial pendulum orbit starting at $\phi = \beta$, ending at $\phi = 2\pi - \alpha$ in the phase space. Such a cross-section shape can be characterised by the eight following characteristic points M, with the corresponding coordinates (η, ζ) given by (2.15). We first choose the reference point M_0 as the origin $(0, 0)$ and the other points are

$$M_{2\pi}, \quad \eta_1 = \eta(2\pi) = -\Lambda_c, \quad \zeta_1 = 0, \tag{3.35}$$

$$M_\beta, \quad \eta_\beta = \eta(\beta), \quad \zeta_\beta = \zeta(\beta), \tag{3.36}$$

$$M_{\pi/2}, \quad \eta^+_{tip} = \eta\left(\frac{\pi}{2}\right), \quad \zeta^+_{tip} = \zeta\left(\frac{\pi}{2}\right), \tag{3.37}$$

$$M_\pi, \quad \eta_{top} = \eta(\pi), \quad \zeta_{top} = z(\pi), \tag{3.38}$$

$$M_{3\pi/2}, \quad \eta^-_{tip} = \eta\left(\frac{3\pi}{2}\right), \quad \zeta^-_{tip} = \zeta\left(\frac{3\pi}{2}\right) = \zeta^+_{tip}, \tag{3.39}$$

$$M_\alpha, \quad \eta_\alpha = \eta(2\pi - \alpha), \quad \zeta_\alpha = \zeta(2\pi - \alpha). \tag{3.40}$$

The last point M_{bott} is located at the bottom of the wedge and has the following coordinates:

$$\eta_{bott} = \eta_\alpha + \frac{\cos\alpha}{\sin(\alpha+\beta)}[(\eta_\beta - \eta_\alpha)\sin\beta - (\zeta_\beta - \zeta_\alpha)\cos\beta], \tag{3.41}$$

$$\zeta_{bott} = \zeta_\alpha - \frac{\sin\alpha}{\sin(\alpha+\beta)}[(\eta_\beta - \eta_\alpha)\sin\beta - (\zeta_\beta - \zeta_\alpha)\cos\beta] \equiv -H_{bott}(\alpha, \beta, m). \tag{3.42}$$

Note that the points M_0 and $M_{2\pi}$ are located inside the cross-section, they do not belong to the boundary of the cross-section and serve as known references.

Using the Green–Riemann formula, we can exactly compute the cross-sectional area of the cylinder by an integration along Γ, the closed curve $\Gamma = \Gamma_0 \cup \Gamma_\alpha \cup \Gamma_\beta$ with positive orientation, that is, using $S_{tot} = -\oint_\Gamma \zeta \, \mathrm{d}\eta$,

$$S_{tot} = -\int_\beta^{2\pi-\alpha} \zeta(\varphi)\frac{\mathrm{d}\eta}{\mathrm{d}\varphi}(\varphi)\,\mathrm{d}\varphi - \int_{\Gamma_\alpha} \zeta^{(\alpha)}\,\mathrm{d}\eta^{(\alpha)} - \int_{\Gamma_\beta} \zeta^{(\beta)}\,\mathrm{d}\eta^{(\beta)}, \tag{3.43}$$

with $(\eta^{(\alpha)}, \zeta^{(\alpha)})$ and $(\eta^{(\beta)}, \zeta^{(\beta)})$ straightforward parameterisations of the line segments Γ_α and Γ_β, respectively, connecting M_α to M_{bott} and M_{bott} to M_β (see figure 5). This yields the expression for the total cross-sectional area $S_{tot}(m, \alpha, \beta)$,

$$\begin{aligned} S_{tot}(m, \alpha, \beta) \;=\; & -\frac{1}{m}\left\{2(m-2)\left[F\left(\pi - \frac{\alpha}{2}\middle| m\right) - F\left(\frac{\beta}{2}\middle| m\right)\right]\right. \\ & \left. + 4\left[E\left(\pi - \frac{\alpha}{2}\middle| m\right) - E\left(\frac{\beta}{2}\middle| m\right)\right]\right\} \\ & - \frac{1}{2}[(\eta_{bott} - \eta_\alpha)(\zeta_\alpha + \zeta_{bott}) + (\eta_\beta - \eta_{bott})(\zeta_{bott} + \zeta_\beta)], \end{aligned} \tag{3.44}$$

with expressions of η_α, η_β, η_{bott}, ζ_α, ζ_β, ζ_{bott} given by (2.14) and (3.35)–(3.42), which yield an explicit expression for the cross-sectional area, for given parameter m and angles α and β. Note that the dependence of S_{tot} on m is monotonic, so that the

relationship between both quantities is unequivocal. In the flat substrate case, for a given cross-sectional area value S, the interface has translational invariance in the y-direction if the starting point $M(s=0)$ is not specified. In contrast, in the wedge case, the relative position of the interface to M_{bott} is unequivocal, once the cross-sectional area S_{tot} is set.

In the following, we will focus on the symmetrical case, namely $\alpha = \beta$. We will again study the dispersion relation of our system in the framework of the Saint-Venant equations (see (3.16), (3.17) and below), that is to say, in the non-dispersive limit. We will only retain the partial derivatives of order zero in x, i.e. only the quadratic terms in k, in the dispersion relation (3.25). Possible instabilities will appear at small wavenumber.

The presence of the symmetrical substrate adds a supplementary term to the expression of the hydrostatic pressure given by (3.15); due to the presence of the wedge underneath the liquid cap, the position of the interface now reads, on top of the drop

$$\zeta_{top}(x,\, t) = \Delta Z_{max}(x,\, t) + H_{bott}(x,\, t), \tag{3.45}$$

so that we can now write

$$\frac{1}{\rho}\partial_x \bar{p} = g\partial_x[\Delta Z_{max}(x,\, t) + H_{bott}(x,\, t)] + \frac{\sigma}{\rho}\partial_x[\kappa_{top}(x,\, t)]. \tag{3.46}$$

Equation (3.44) allows us to compute the derivative of the cross-sectional area with respect to the parameter m, so that the effective speed of propagation of waves along a sessile cylindrical drop above a wedge can be explicitly computed, using

$$c_{eff}^2(m,\, \alpha,\, \beta) = g\ell_c \left[\frac{S_{tot}(\alpha,\, \beta,\, m)}{\dfrac{\partial S_{tot}(\alpha,\, \beta,\, m)}{\partial m}}\right]\left[\frac{1}{\ell_c}\frac{\partial H_{bott}}{\partial m} - m^{-3/2}\right], \tag{3.47}$$

for a parameter m corresponding to that of the drop at rest, knowing that $\beta = \alpha$. The full explicit expression of $c_{eff}^2(m,\, \alpha,\, \beta)$ is overly complicated to be written down. However, one important remark is that the negative factor $-m^{-3/2}$ yielding the Plateau–Rayleigh instability in the case of a flat substrate can be compensated by the additional positive term $\ell_c^{-1} \times [\partial H_{bott}/\partial m]$ stemming from the presence of the non-flat substrate underneath the sessile drop, provided it is sufficiently large.

At given angle α, the quantity $(1/\ell_c)(\partial H_{bott}/\partial m) - m^{-3/2}$ is negative for small values of m. It becomes positive when m is larger than a critical value $m_c = 1 - \mu_c$. This latter quantity can be numerically computed and its dependence on the angle α is plotted in figure 6. For $\alpha = 0$, i.e. for a flat substrate, the cylinder is unstable whatever its cross-section may be (see § 3.4.2).

In the following, in order to illustrate all these calculations in a meaningful way, we perform some approximate computations and discuss their validity. They will come in handy for comparisons with the experimental results (see § 4).

As a reminder, we are dealing with the symmetrical case ($\alpha = \beta$) and we will make the following hypotheses: the angle α is supposedly small and the parameter $m = 1 - \mu$ is close to 1, i.e. large flattened cross-sections are considered. We can approximate the geometrical properties of our system by considering a cap (given by the shape of a sessile drop on a flat surface) placed on top of a symmetrical triangle (see figure 7*a*).

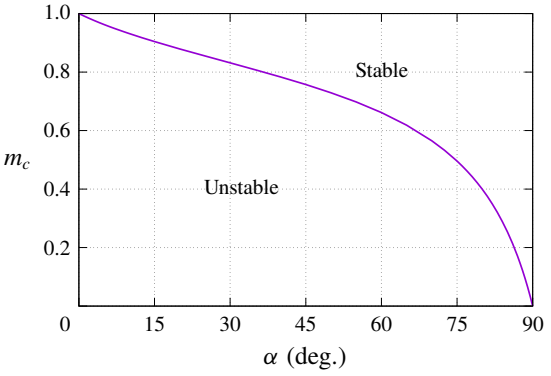

FIGURE 6. Dependence of the critical parameter m_c on the angle α of a symmetrical V-shaped substrate ($\alpha = \beta$). For positive α, large drops (m close to 1) are stable as long as $m > m_c(\alpha)$.

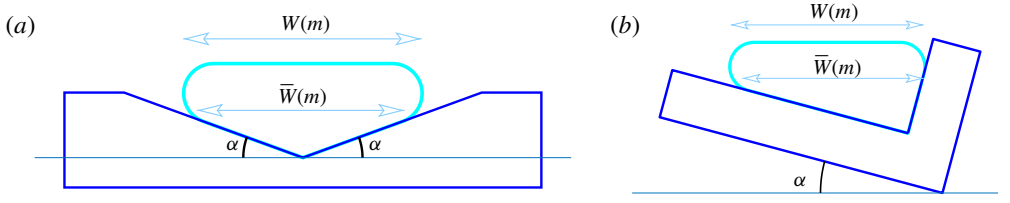

FIGURE 7. Geometry of the two different substrate shapes used in our experiments. (*a*) V-shaped symmetrical channel. (*b*) L-shaped asymmetrical channel. For a given parameter m, $W(m)$ is the width of the sessile cap, whereas $\overline{W}(m)$ denotes the width of the triangular cross-section, which can somehow be approximated by the wetted length $\Lambda_c(m)$ (see text).

We have the following approximate quantities, using the asymptotic formulas of § 2.2,

(i) for the sessile cap:

  (*a*) width $W(m) \simeq \Delta Y_{max} \simeq \ell_c[-\log(1-m) + \mathscr{C}_1]$;

  (*b*) cross-sectional area $S_{cap}(m) \simeq W(m) \times \Delta Z_{max}(m) \simeq 2\ell_c^2[-\log(1-m) + \mathscr{C}_1]$;

(ii) for the triangle:

  (*a*) width $\overline{W}(m) \simeq \Lambda_c(m) \simeq \ell_c[-\log(1-m) + \mathscr{C}_2]$;

  (*b*) height $H_{bott}(m) \simeq \frac{1}{2}\overline{W}(m)\tan\alpha$;

  (*c*) cross-sectional area $S_0 = \frac{1}{4}\overline{W}(m)^2\tan\alpha$.

The total cross-sectional area is

$$S_{tot}(m) \simeq S_{cap}(m) + S_0(m) \simeq 2\ell_c^2 W(m) + \frac{1}{4}\overline{W}(m)^2\tan\alpha,$$
$$\simeq \ell_c^2\left[2(-\log(1-m) + \mathscr{C}_1) + \frac{\tan\alpha}{4}[-\log(1-m) + \mathscr{C}_2]^2\right], \quad (3.48)$$

so that

$$\frac{\partial S_{tot}}{\partial m}(m) = \ell_c^2\frac{\tan\alpha\,[\mathscr{C}_2 - \log(1-m)] + 4}{2(1-m)}. \quad (3.49)$$

α (deg.)	3°	5°	10°	15°	20°	30°	45°
μ_c (exact)	0.0237	0.0376	0.0685	0.0958	0.121	0.168	0.243
$\tilde{\mu}_c$ (approximation)	0.0252	0.0412	0.0788	0.114	0.149	0.218	1/3
$\Delta Y_{max}(\mu_c)/\ell_c$	3.65	3.21	2.66	2.36	2.15	1.87	1.56
$S(\mu_c)/\ell_c^2$	5.45	4.70	3.87	3.51	3.33	3.20	3.18

TABLE 1. Values of critical μ_c together with corresponding non-dimensional values of horizontal extension $\Delta Y_{max}(\mu_c)/\ell_c$ and of cross-sectional area $S(\mu_c)/\ell_c^2$, for a symmetrical V-shaped substrate. The values in the framework of the approximate computations (namely $\tilde{\mu}_c$, see § 3.5) are added for comparison.

The effective wave celerity then reads, using (3.47),

$$c_{eff}^2(m) = g\ell_c \left[\frac{S_{tot}(m)}{\dfrac{\partial S_{tot}}{\partial m}(m)}\right] \left\{+\frac{\tan\alpha}{2\mu} - 1 - \frac{3\mu}{2} + O(\mu^2)\right\}, \tag{3.50}$$

with

$$\left[\frac{S_{tot}(m)}{\dfrac{\partial S_{tot}}{\partial m}(m)}\right] = 2(1-m)\frac{2[\mathscr{C}_1 - \log(1-m)] + \dfrac{\tan\alpha}{4}[\mathscr{C}_2 - \log(1-m)]^2}{\tan\alpha[\mathscr{C}_2 - \log(1-m)] + 4}. \tag{3.51}$$

If we have $\alpha = 0$ (flat substrate), we recover $c_{eff}^2 < 0$, corresponding to an unstable drop, whatever its size may be. For small values of μ and $\tan\alpha \neq 0$, the drop is stable, provided $\tan\alpha/2\mu - 1 - \frac{3}{2}\mu > 0$, that is

$$\mu < \tilde{\mu}_c = \frac{\sqrt{1 + 3\tan\alpha} - 1}{3}. \tag{3.52}$$

As a comparison, in the experiments we present in the next section, we have typical values of width equal to $7.5\,\ell_c$, that corresponds to a parameter $\mu_{exp} \simeq 5 \times 10^{-4}$, which satisfies the stability criterion.

Note that up to $\alpha \simeq 10°$, our approximations in terms of $\log\mu$ are valid for calculating the critical threshold. For large angles α, this approximate threshold value is arguable. One has to resort to the exact analytical computations presented previously. However, comparisons between these approximations and actual exact results remain surprisingly good, the relative errors being no greater than 30 % for α up to 45° (see table 1).

We can compute an ultimate term, that of (3.51), in the limit $\mu \to 0^+$, that reads

$$\left[\frac{S_{tot}}{\dfrac{\partial S_{tot}}{\partial m}}\right] \underset{\mu\to 0^+}{\sim} 2\mu \frac{\dfrac{\tan\alpha}{4}\log^2\mu - 2\log\mu}{-\tan(\alpha)\log\mu + 4} \underset{\mu\to 0^+}{\sim} -\frac{1}{2}\mu\log\mu. \tag{3.53}$$

We recover the expression of the wave celerity c_{eff},

$$c_{eff}^2 = -g\ell_c\frac{\tan\alpha}{4}\log\mu = g\frac{H_{bott}}{2}, \tag{3.54}$$

in the large cross-section limit as explained in § 3.2 (see (3.10)). It is the gravity wave speed directly given by the Saint-Venant equations, in the case of a symmetrical channel of angle α, in the absence of capillarity. The presence of a sessile cap is of no importance in this limit and it thus can be disregarded, as one would have expected it to be.

4. Experimental comparisons

4.1. *Experimental set-up*

In this section, we present an experimental characterisation of the varicose waves propagating along cylindrical drops, when deposited upon superhydrophobic substrates. The critical volume at which breakup of these drops occurs is studied as well. In order to distinguish the theoretical liquid cylinder shape from its experimental realisation, we use the term 'drop' in this section to denote a slender volume of liquid deposited upon a non-flat substrate with translational invariance.

For this study, we use two different substrates. The first one is a symmetrical V-shaped Dural channel with angle $\alpha = 10°$. The second one is an L-shaped Dural channel, placed upon a levelling table, so that it can be tilted by an angle α, set from 0° up to 45° (see the schematic of substrate cross-section in figure 7). The surface of these substrates is treated using Rust-Oleum NeverWet, so that the wetting conditions (contact angle around 160°) can be considered as superhydrophobic (see Gupta, Vaikuntanathan & Siakumar 2016). Both channels are 50 cm long. On either of them, a controlled volume of distilled water is deposited and stretched from one end to the other end of the channel. If the deposited volume is sufficiently large, we can pin such long drops at both ends of the channel without breakup.

In order to study the propagation of varicose waves along these drops, we force one end of the drop using a shaker at swept frequencies (1–25 Hz) (see figure 8*a*). Two photographs are shown as an illustration in figure 8(*b*,*c*). The plate connected to the shaker can be seen at the right-hand side of the photographs. The photographs correspond to excited drops of volume equal to 40 ml, deposited on the symmetric V-shaped substrate and the non-symmetrical L-shaped substrate, respectively, with a tilt angle $\alpha = 10°$. In the symmetrical case, constriction modes are clearly visible near the shaker, whereas in the non-symmetrical case, only the deformations of one side of the drop can be captured, for deformations of the border of the drop at the steepest side of the substrate are too small to be visible. We then naturally focus on the interface located on the smallest slope of the substrate. The deformation of the border of the drop and consequently the position $\eta(x, t)$ of the border of the interface is recorded from above using a digital camera at 50 f.p.s. (AVT Manta G223). The interface position is numerically reconstructed using an algorithm of contour detection based on the change in the colour gradient, with a 0.03 mm accuracy: we record images of a region of interest of a border of the drop. Suppose the images have resolution $\mathtt{Nx} \times \mathtt{Ny}$, at all discrete x-coordinates $(x_i)_{1 \leqslant i \leqslant \mathtt{Nx}}$, we locate the minimum of intensity in the y-direction (for $1 \leqslant j \leqslant \mathtt{Ny}$), using polynomial interpolations of the discrete values in this direction. The procedure is performed at each discrete time t_k ($1 \leqslant k \leqslant \mathtt{Nt}$), so that we obtain a discrete signal $\eta(x_i, t_k)$. Last, we compute the position at rest $\eta_0(x_i)$ of the interface, using the same procedure.

4.2. *Experimental results*

From the camera recordings, we compute the spatio-temporal spectrum $S(k, f)$ of the disturbed interface by performing fast Fourier transforms on the difference

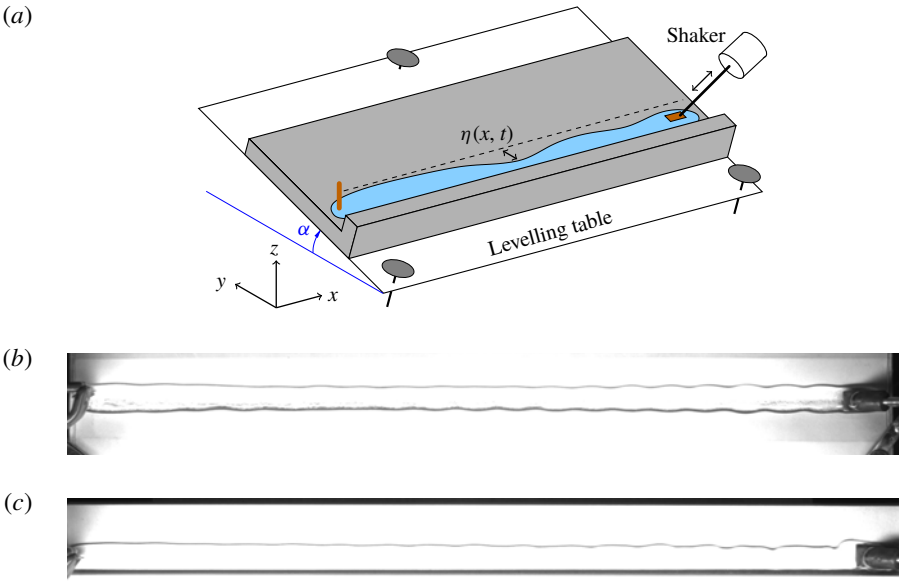

FIGURE 8. (*a*) Schematic of the experimental set-up. Top views of experiments of shaken drops of volume 40 ml (*b*) on a symmetrical V-shaped substrate (of angle $\alpha = 10°$) and (*c*) on a non-symmetrical L-shaped substrate tilted by an angle $\alpha = 10°$. They are lit so that the border of the drop is clearly visible for numerical treatments. Varicose modes, i.e. constriction modes, are clearly visible near the shaker. They are symmetrical in the V-shaped case. In contrast, due to the asymmetry of the L-shaped substrate, only the constrictions of the interface border located at the gentle slope side (upper side of the image) are clearly visible. They propagate and vanish far from the shaker because of dissipation and dispersion.

$\eta(x_i, t_k) - \eta_0(x_i)$. The spatial resolution is 0.252 mm pixels, and we use a typical image resolution `Nx` equal to 1690 pixels. As for the temporal sampling, the typical recording duration is 2 minutes, which yields a typical number of time samples `Nt` ~ 6000. Several branches can be identified from the spatio-temporal spectra (see figure 9). We focus here on the lowest branch, which goes to zero when $k \to 0$ (namely the varicose branch). Other branches (characterised by cutoff frequencies at $k = 0$) are related to the other modes of wave propagation, the very first upper branch being related to sloshing motion (namely sinuous waves).

From the value of deposited volume, V_0, we can deduce the value at rest of the cross-sectional area, $S_{tot} = V_0/L$, with L, the length of the cylinder. Using the expression (3.44) of $S_{tot}(m)$, we can estimate the corresponding parameter m, hence the width $W(m)$. From these data, we can evaluate c_{eff} and plot $f(k) = (1/2\pi)c_{eff}k$ (the non-dispersive long-wavelength regime given by the Saint-Venant formalism) and compare them to the experimental measurements. The small-wavelength regime (dispersive regime) together with the sinuous modes will be discussed in a future article.

4.2.1. *Case of the V-shaped symmetrical substrate*

We now start with the spatio-temporal spectra of an elongated drop, placed upon a superhydrophobic symmetric V-shaped substrate, for four different volumes (23 ml,

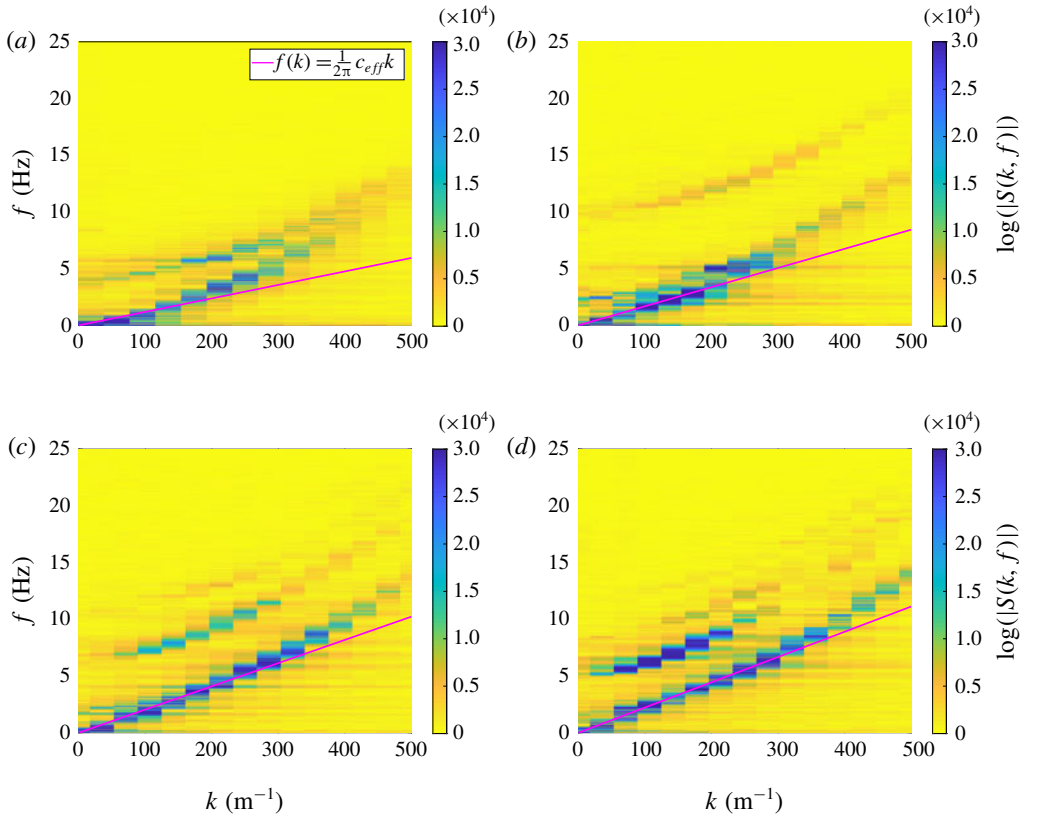

FIGURE 9. Spatio-temporal spectra of elongated drops, on a superhydrophobic symmetric V-shaped substrate with an angle $\alpha = 10°$, for four different volumes V. We have superimposed the linear relation $f(k) = (1/2\pi)c_{eff}k$ with c_{eff} calculated using (3.50) and (3.51). (*a*) $V = 23$ ml, $c_{eff} = 7.47$ cm s^{-1}; (*b*) $V = 40$ ml, $c_{eff} = 10.60$ cm s^{-1}; (*c*) $V = 60$ ml, $c_{eff} = 12.86$ cm s^{-1}; (*d*) $V = 80$ ml, $c_{eff} = 13.98$ cm s^{-1}. The smaller the volume, the smaller the slope at origin, namely the effective celerity of long wavelength varicose modes. Below a critical volume $V_c \simeq 15$ ml, the drop becomes unstable. The agreements are excellent. The secondary branches correspond to other modes of propagation (in particular, sloshing modes).

40 ml, 60 ml, 80 ml) at fixed angle $\alpha = 10°$. These spectra are plotted in figure 9. The smaller the volume, the smaller the slope at origin, which is the celerity of surface waves c_{eff}. We compare this experimental slope to its analytical value found using the Saint-Venant formalism, in the large drop limit (see (3.50) and (3.51)), for a parameter m deduced from the value of deposited volume of water. The agreement is excellent (even better if we use the exact computations given by (3.47)). The larger the volume, the steeper the slope, that is the larger the value of c_{eff}.

We can clearly distinguish the existence of upper branches. The very first branch corresponds to sloshing modes. Its cutoff frequency depends on the volume of the drop. The larger the volume, the smaller the cutoff frequency. This point will be discussed in a future article.

4.2.2. *Case of non-symmetrical substrate: L-shaped substrate or inclined V-shaped substrate*

We now turn to the asymmetrical case which corresponds to a cap placed on top of an asymmetrical right-angled triangle (see figure 7*b*). The triangle properties will satisfy the following properties: small angle α and steep angle $\beta = (\pi/2) - \alpha$, width $W(m)$ supposedly large. The properties of the sessile cap are identical to those of the symmetrical case. As for the triangle, we can approximate the length of its hypotenuse $\overline{W}(m)$, with ΔY_{max} minus the length of one of the tip of liquid protruding above the wetted area, which was approximated as being $\ell_c/2(\mathscr{C}_1 - \mathscr{C}_2)$. Here, $\overline{W}(m)$ turns out to be somehow equivalent to the mean value of ΔY_{max} and Λ_c. We set $\mathscr{C}_3 = \frac{1}{2}(\mathscr{C}_1 + \mathscr{C}_2)$, so that the triangle has the following properties:

(i) width $\overline{W}(m) \simeq \frac{1}{2}[W(m) + \Lambda_c] = \ell_c[-\log(1-m) + \mathscr{C}_3]$;

(ii) height $H_{bott}(m) \simeq \frac{1}{2}\overline{W}(m) \sin 2\alpha$; and

(iii) cross-sectional area $S_0 = \frac{1}{4}\overline{W}(m)^2 \sin 2\alpha$.

Therefore, we can compute the effective propagation speed

$$c_{eff}^2(m) = g\ell_c \left[\frac{S_{tot}(m)}{\dfrac{\partial S_{tot}}{\partial m}(m)}\right] \left\{+\frac{\sin 2\alpha}{2\mu} - 1 - \frac{3\mu}{2} + O\left(\mu^2\right)\right\}, \tag{4.1}$$

with

$$\left[\frac{S_{tot}(m)}{\dfrac{\partial S_{tot}}{\partial m}(m)}\right] = 2(1-m)\frac{2[\mathscr{C}_1 - \log(1-m)] + \dfrac{\sin 2\alpha}{4}[\mathscr{C}_3 - \log(1-m)]^2}{\sin 2\alpha[\mathscr{C}_3 - \log(1-m)] + 4}. \tag{4.2}$$

For a fixed volume of 40 ml, we show the spatio-temporal spectra for two different angles (10° and 30°) in figure 10. The values of the parameter m used for the following comparisons between experiments and theory are set by the value of the deposited volume of water. For $\alpha = 10°$, the agreement between the experimental slope at origin and c_{eff} given by (4.1) is excellent, whereas in order to capture the correct theoretical value of c_{eff} at angle $\alpha = 30°$, we resort to exact calculations given by (3.47) and we can see that the agreement is excellent as well.

Last, we have performed an experiment using our V-shaped substrate tilted by an angle 5°, that corresponds to the asymmetrical case $\alpha = 5°$ and $\beta = 15°$. It is displayed in figure 10(*c*) together with the Saint-Venant dispersion relation $f(k) = (1/2\pi)c_{eff}k$, where c_{eff} is computed using (3.47), with an excellent agreement.

4.2.3. *Experimental threshold of breakup*

Section 3.5 was devoted to the critical value of the parameter μ (hence m) at which instability occurs, that is when c_{eff}^2 changes its sign, from positive to negative as volume decreases (that is when the parameter μ increases). In order to experimentally confirm these predictions, we pin both ends of a large controlled volume of water, deposited upon our superhydrophobic substrates (V-shaped substrate together with L-shaped substrate that we tilt at angle α). We progressively and carefully pump controlled volumes of water out from one end of the cylinder, of length L, using a syringe with a very sharp needle in order to minimise meniscus effects. We deduce

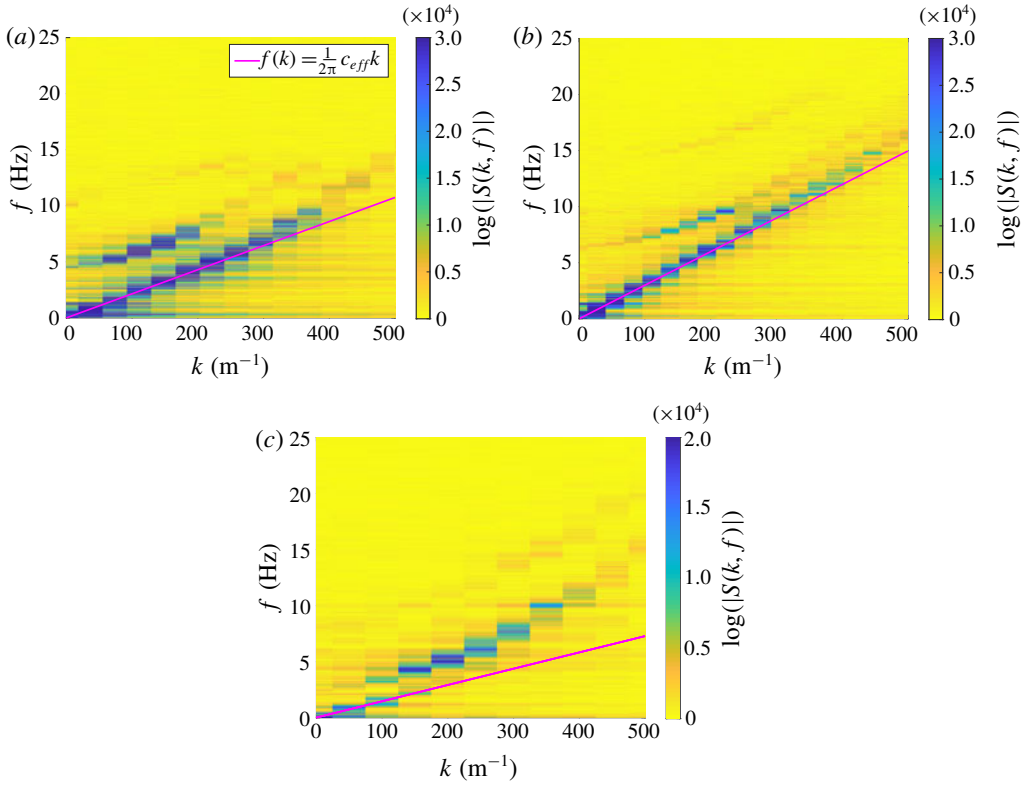

FIGURE 10. Spatio-temporal spectra of elongated drops, on a superhydrophobic asymmetrical L-shaped substrate, for a volume equal to 40 ml and two different angles α. We have superimposed the linear relation $f(k) = (1/2\pi)c_{eff}k$. (*a*) $\alpha = 10°$, $c_{eff} = 13.5$ cm s^{-1}; (*b*) $\alpha = 30°$, $c_{eff} = 18.8$ cm s^{-1}. The larger the angle, the larger the slope, namely the celerity of varicose modes. And last, (*c*) spectrum of an elongated drop, on a superhydrophobic asymmetrical tilted V-shaped substrate corresponding to the case $\alpha = 5°$ and $\beta = 15°$, for volume $V = 40$ ml. We have $c_{eff} = 9.13$ cm s^{-1}. In all the cases, the secondary branches correspond to other modes of propagation (for instance, sloshing modes).

the remaining deposited volume, down to a critical volume at which the drop breaks up. The (slow) pinch-off is located about the centre of the cylinder and retraction of both remaining halves eventually occurs, owing to surface tension (see supplementary movies, long shot and close-up, in the case of the symmetrical V-shaped substrate which are available at https://doi.org/10.1017/jfm.2020.114). The critical volume V_c^{exp} allows us to obtain the critical cross-sectional area S_c^{exp} of the drop ($S_c^{exp} = V_c^{exp}/L$), hence the critical value μ_c^{exp}, using (3.44). We compare this experimental value to the theoretical one in table 2. The breakup of the drops systematically occurs at volumes approximately 1.3 times larger than the predicted theoretical volumes for a given substrate geometry.

At this limit regime, we have to stress that the system becomes very sensitive to any external perturbations such as the vibrations caused by the pumping procedure. Moreover, the translational invariance is broken because of the meniscus created by our pinning procedure. It induces a bulge at both tips of the drop, so that the effective

	Substrate	V-shaped	L-shaped	L-shaped	L-shaped	L-shaped
	α	10°	10°	20°	30°	45°
Theory:	μ_c	0.0685	0.118	0.184	0.223	0.243
	$\frac{1}{\ell_c^2}S_c$	3.87	3.95	3.43	3.24	3.18
Experiments:	μ_c^{exp}	0.0381	0.0710	0.101	0.131	0.150
	$\frac{1}{\ell_c^2}S_c^{exp}$	4.97	4.90	4.54	4.20	4.07

TABLE 2. Values of the critical thresholds found in our experiments, in the cases of the symmetrical V-shaped substrate ($\alpha = 10°$), and the non-symmetrical L-shaped substrates. Here, we have $\ell_c = 2.5$ mm.

volume per unit length, i.e. the effective cross-sectional area of the cylindrical part of our drop, turns out to be lower than that measured in our procedure. Using a longer channel would certainly help alleviate this discrepancy.

5. Conclusion

In this article, we have computed the exact shape of the cross-section of a cylindrical (i.e. assuming translational invariance) sessile drop of liquid deposited upon a superhydrophobic substrate, taking into account the flattening effect of gravity. The substrate geometry was supposed either flat and horizontal or that of a wedge. Using an analogy with the rotation motion of a pendulum, we show how the shape is related to the value of the cross-sectional area (in capillary length unit). When the cross-sectional area is small, the cross-section is nearly a circle, whereas the large cross-section shapes more or less resemble oblong pills. In the wedge-shaped substrate case, the cross-section is equivalent to that of a liquid cap placed upon a liquid wedge.

We have used the inviscid Saint-Venant equations, in order to study the stability of such sessile drops, in terms of the square of an effective wave propagation speed, c_{eff}^2, of the varicose modes of the drop (namely constriction modes). In this framework, we have shown that in the case of a flat substrate, such drops are linearly unstable as the values of c_{eff}^2 are always negative, whatever the cross-sectional area may be. This regime corresponds to the well known Plateau–Rayleigh instability in the case of circular cross-sections. In contrast, placed upon a wedge-shaped substrate, such drops can become stable, corresponding to a positive sign of c_{eff}^2, provided the cross-sectional area of the drop is sufficiently large.

These theoretical predictions have been experimentally tested with an excellent agreement, using specifically designed superhydrophobic substrates: a symmetrical V-shaped substrate and a non-symmetrical L-shaped substrate. Both can be tilted and using the L-shaped substrate allows us to tune the geometry and reach a wide range of non-symmetrical wedge angles. By measuring the spatio-temporal spectra of the deformation of the border of the drop when excited by a shaker, we have evidenced multiple branches corresponding to the dispersion relations of the various wave modes ($\omega = f(k)$ with ω, the angular frequency and k the wavenumber). Our theoretical Saint-Venant calculations correspond to the non-dispersive regime of the lowest branch that goes to zero in the limit $k \to 0$. The slope at origin is equal to the expected value of c_{eff}.

Note that these experimental results are equivalent to the spectra found in previous work related to the wave propagation along levitating cylinders (Perrard *et al.* 2015). The Saint-Venant formalism is only valid in the $k \to 0$-limit of the lowest branch. The dispersive effects of the varicose modes cannot be captured by this formalism. It is of course unfit to capture the upper branches. The problem of the full dispersive regime of the varicose modes together with the characterisation of the sinuous modes (corresponding to sloshing motion) is beyond the scope of this article. A future article will be devoted to this problem.

Acknowledgements

C.-T.P. thanks C. Mezui for preliminary experiments, M. Receveur and A. Grados for technical support. The authors gratefully thank laboratoire Matière et Systèmes Complexes (MSC) and Laboratoire d'Informatique pour la Mécanique et les Sciences de l'Ingénieur (LIMSI) for their valuable material and financial support. We thank the anonymous referee who indicated to us the references from Lamb (1928), Ku *et al.* (1968) and McCuan (2017), which we were unaware of. This work has benefited from no other funding whatsoever.

Declaration of interests

The authors report no conflict of interest.

Supplementary movies

Supplementary movies are available at https://doi.org/10.1017/jfm.2020.114.

REFERENCES

AMINI, G. & DOLATABADI, A. 2011 Capillary instability of elliptic liquid jets. *Phys. Fluids* **23**, 084109.

AMINI, G., LV, L., DOLATABADI, A. & IHME, M. 2014 Instability of elliptic liquid jets: temporal linear stability theory and experimental analysis. *Phys. Fluids* **26**, 114105.

ARKHIPENKO, V. I., BARKOV, Y. D., BASHTOVOI, V. G. & KRAKOV, M. S. 1980 Investigation into the stability of a stationary cylindrical column of magnetizable liquid. *Fluid Dyn.* **15**, 477–481.

BIRNIR, B., MERTENS, K., PUTKARADZE, V. & VOROBIEFF, P. 2008 Morphology of a stream flowing down an inclined plane. Part 2. Meandering. *J. Fluid Mech.* **603**, 401–411.

BOSTWICK, J. B. & STEEN, P. H. 2010 Stability of constrained cylindrical interfaces and the torus lift of Plateau–Rayleigh. *J. Fluid Mech.* **647**, 201–219.

BOSTWICK, J. B. & STEEN, P. H. 2018 Static rivulet instabilities: varicose and sinuous modes. *J. Fluid Mech.* **837**, 819–838.

COUVREUR, S. 2013 Instabilités de filets liquides sur plan incliné. PhD thesis, Université Paris Diderot.

DAERR, A., EGGERS, J., LIMAT, L. & VALADE, N. 2011 General mechanism for the meandering instability of rivulets of Newtonian fluids. *Phys. Rev. Lett.* **106**, 184501.

DAVIS, S. H. 1980 Moving contact lines and rivulet instabilities. Part 1. The static rivulet. *J. Fluid Mech.* **98**, 225–242.

DECOENE, A., BONAVENTURA, L., MIGLIO, E. & SALERI, F. 2009 Asymptotic derivation of the section-averaged shallow water equations. *Math. Models Meth. Appl. Sci.* **19**, 387–417.

DIEZ, J. A., GONZÁLEZ, A. G. & KONDIC, L. 2009 On the breakup of fluid rivulets. *Phys. Fluids* **21** (8), 082105.

DUCLAUX, V., CLANET, C. & QUÉRÉ, D. 2006 The effects of gravity on the capillary instability in tubes. *J. Fluid Mech.* **556**, 217–226.

GOREN, S. L. 1962 The instability of an annular thread of fluid. *J. Fluid Mech.* **12**, 309–319.

GUPTA, R., VAIKUNTANATHAN, V. & SIAKUMAR, S. 2016 Superhydrophobic qualities of an aluminum surface coated with hydrophobic solution NeverWet. *Colloids Surf.* A **500**, 45–53.

GUTMARK, E. J. & GRINSTEIN, F. F. 1999 Flow control with noncircular jets. *Annu. Rev. Fluid Mech.* **31**, 239–272.

KU, T. C., RAMSEY, J. H. & CLINTON, W. C. 1968 Calculation of liquid droplet profiles from closed-form solution of Young–Laplace equation. *IBM J. Res. Dev.* **12**, 441–447.

LAMB, H. 1928 *Statics, including Hydrostatics and the Elements of the Theory of Elasticity*, 3rd edn. Cambridge University Press.

LANDAU, L. D. & LIFSCHITZ, E. M. 1987 *Fluid Mechanics*, 2nd edn. Pergamon.

LANGBEIN, D. 1990 The shape and stability of liquid menisci at solid edges. *J. Fluid Mech.* **213**, 251–265.

MCCUAN, J. 2017 The stability of cylindrical pendant drop. In *Memoirs of the American Mathematical Society*, **250** (1189), doi:10.1090/memo/1189.

MERTENS, K., PUTKARADZE, V. & VOROBIEFF, P. 2005 Morphology of a stream flowing down an inclined plane. Part 1. Braiding. *J. Fluid Mech.* **531**, 49–58.

MICHAEL, D. H. & WILLIAMS, P. G. 1977 The equilibrium and stability of sessile drops. *Proc. R. Soc. Lond.* A **354**, 127–136.

MORA, S., PHOU, T., FROMENTAL, J.-M., PISMEN, L. M. & POMEAU, Y. 2010 Capillary driven instability of a soft solid. *Phys. Rev. Lett.* **105**, 214301.

MORRIS, P. J. 1988 Instability of elliptic jets. *AIAA J.* **26**, 172–178.

MYERS, T. G., LIANG, H. X. & WETTON, B. 2004 The stability and flow of a rivulet driven by interfacial shear and gravity. *Intl J. Nonlinear Mech.* **39**, 1239–1249.

NAKAGAWA, T. 1992 Rivulet meanders on a smooth hydrophobic surface. *Intl J. Multiphase Flow* **18**, 455–463.

NAKAGAWA, T. & SCOTT, J. C. 1984 Stream meanders on a smooth hydrophobic surface. *J. Fluid Mech.* **149**, 88–99.

PERRARD, S., DEIKE, L., DUCHÊNE, C. & PHAM, C.-T. 2015 Capillary solitons on a levitated medium. *Phys. Rev.* E **92**, 011002(R).

PLATEAU, J. 1849 Recherches expérimentales et théoriques sur les figures d'une masse liquide sans pesanteur. *Mémoires de l'Académie royale des sciences, des lettres et des beaux arts de Belgique* **23**, 1–50.

PLATEAU, J. 1873 *Statique expérimentale et théorique des liquides soumis aux seules forces moléculaires*. Gauthier-Villars.

QUINN, W. R. 1992 Streamwise evolution of a square jet cross section. *AIAA J.* **30**, 2852–2857.

RAYLEIGH, LORD 1878 On the instability of jets. *Proc. Lond. Math. Soc.* **10**, 4–13.

RAYLEIGH, LORD 1879 On the capillary phenomena of jets. *Proc. R. Soc. Lond.* **29**, 71–97.

RAYLEIGH, LORD 1892*a* On the instability of a cylinder of viscous liquid under capillary force. *Philos. Mag.* **34**, 145–154.

RAYLEIGH, LORD 1892*b* On the instability of cylindrical fluid surfaces. *Philos. Mag.* **34**, 177–180.

ROMAN, B., GAY, C. & CLANET, C. 2003 Pendulum, drops and rods: an analogy. Available at: https://www.researchgate.net/publication/237480399_Pendulum_Drops_and_Rods_a_physical_analogy.

ROY, V. & SCHWARTZ, L. W. 1999 On the stability of liquid ridges. *J. Fluid Mech.* **291**, 293–318.

SAINT-VENANT, A. J. C. B. DE 1871 Théorie du mouvement non permanent des eaux, avec application aux crues des rivières et a l'introduction de marées dans leurs lits. *C. R. Acad. Sci.* **73**, 147–154 and 237–240.

SAVART, F. 1833 Mémoire sur la constitution des veines liquides lancées par des orifices circulaires en mince paroi. *Ann. Chim. Phys.* **53**, 337–386.

SCHMUKI, P. & LASO, M. 1990 On the stability of rivulet flow. *J. Fluid Mech.* **215**, 125–143.

SEKIMOTO, K., OGUMA, R. & KAWASAKI, K. 1987 Morphological stability analysis of partial wetting. *Ann. Phys.* **176**, 359–392.

SPETH, R. L. & LAUGA, E. 2009 Capillary instability on a hydrophilic stripe. *New J. Phys.* **11**, 075024.

STONE, H. A. & LEAL, L. G. 1989*a* The influence of initial deformation on drop breakup in subcritical time-dependent flows at low Reynolds numbers. *J. Fluid Mech.* **206**, 223–263.

STONE, H. A. & LEAL, L. G. 1989*b* Relaxation and breakup of an initially extended drop in an otherwise quiescent fluid. *J. Fluid Mech.* **198**, 399–427.

TAM, C. K. W. & THIES, A. T. 1992 Instability of rectangular jets. *J. Fluid Mech.* **248**, 425–448.

TOMOTIKA, S. 1935 On the instability of a cylindrical thread of a viscous liquid surrounded by another viscous fluid. *Proc. R. Soc. Lond.* A **150**, 322–337.

YANG, L. & HOMSY, G. M. 2007 Capillary instabilities of liquid films inside a wedge. *Phys. Fluids* **19**, 044101.